Numerical Investigation of Multi-rotor Configurations

Jonathan J. Chiew *
Stanford University
Stanford, CA 94305

Michael J. Aftosmis †
NASA Ames Research Center
Moffett Field, CA 94035

The development of a conservative, parallel blade-element rotor model and its implementation into an adaptive Cartesian method is briefly reviewed. The model is first validated and then applied in edgewise forward flight for a variety of configurations. Validation studies comparing torque required for an isolated rotor match XV-15 wind tunnel trends well. Simulations of a simple quadrotor in "×" and "+" configurations are performed, demonstrating how the trailing rotor(s) lose thrust because of unfavorable aerodynamic interactions with the forward rotor(s), while power required remains near constant. A modified "+′" configuration is also examined, where the lateral rotors are brought inboard by 25%. This configuration showed a further 2% performance improvement over the "+" arrangement. ***The final paper will also include validation of a tandem rotor configuration with wind tunnel data as well as results and analysis of unsteady quadcopter simulations. In addition, a 4th configuration*** **(×′)** ***with its aft rotors moved outboard will be analyzed.***

I. Introduction

Multi-rotor vehicles have seen a surge in popularity recently, as advancements in electric motors, battery technology, and controllers have enabled a variety of configurations at multiple scales and prices. Since an electric propulsion system's efficiency is relatively scale-invariant, multi-copters can utilize several smaller, simpler rotors compared to conventional helicopters, particularly if hover endurance is not a primary design requirement.

However, typical multi-rotor designs prioritize configuration simplicity and utilize only low-fidelity aerodynamic analyses or correlations.[1,2] For multi-rotor configurations, much of the recent computational and experimental work on interactional aerodynamics has focused on hover performance,[3,4,5] but these vehicles often spend the majority of their missions in edgewise flight. Luo, Zhu, and Yan proposed an interference model that represented the rotors as circular wings in forward flight but found the assumption of uniform inflow on each rotor to be invalid.[6] They used high-fidelity computational fluid dynamics (CFD) tools to resolve the wake interactions from first principles similar to Hwang, Jung, and Kwon.[7] Unfortunately, these simulations typically require significant high performance computing resources and have long turn-around times because each blade is individually modeled, which lengthens mesh generation time and requires unsteady simulations.

In this work, we utilize a recently developed medium-fidelity rotor aerodynamics model coupled to an adaptive Cartesian Euler solver[8] to analyze several multi-rotor configurations. We begin with a validation study of an isolated rotor in edgewise flight and build up to complete simulations of representative quadcopters.

II. Governing Equations and Numerical Method

The three dimensional Euler equations governing inviscid flow of a calorically perfect gas for a control volume Ω with closed boundary $\partial\Omega$ may be written as

$$\iiint_{\Omega} \frac{\partial \mathbf{U}}{\partial t} dV + \oint_{\partial\Omega} \mathbf{F} \cdot \hat{n}\, dS = \iiint_{\Omega} \mathbf{S}\, dV \tag{1}$$

*Ph.D. Candidate, Dept. of Aeronautics & Astronautics, jchiew@stanford.edu, AIAA Student Member
†Senior Research Scientist, Computational Aerosciences Branch, michael.aftosmis@nasa.gov, AIAA Associate Fellow

where $\mathbf{U}$ is the vector of conserved variables,

$$\mathbf{U} = [\rho, \rho u, \rho v, \rho w, \rho E]^T \tag{2}$$

$\mathbf{F}$ is the flux density tensor,

$$\mathbf{F} = \begin{bmatrix} \rho u & \rho u^2 + p & \rho uv & \rho uw & u(\rho E + p) \\ \rho v & \rho uv & \rho v^2 + p & \rho vw & v(\rho E + p) \\ \rho w & \rho uw & \rho vw & \rho w^2 + p & w(\rho E + p) \end{bmatrix}^T \tag{3}$$

$\hat{n}$ is the outward facing unit normal vector, ρ is the fluid density, u, v, and w are the Cartesian velocity components, p is the fluid pressure, E is the total energy per unit mass, and S is an arbitrary body-force vector.

The rotor model is implemented in a widely used simulation framework which solves the governing equations (1) using a multilevel Cartesian mesh with embedded boundaries.[9] The mesh consists of regular Cartesian hexahedra everywhere, except for a layer of cut cells, in which the cells that contact the geometry are clipped into arbitrarily shaped polyhedra.[10] The spatial discretization uses a second-order, finite volume approach with a weak imposition of boundary conditions. Time-dependent flow solutions utilize dual-time stepping where a Runge-Kutta based multigrid smoother drives an implicit second-order, backward difference time integration scheme similar to Jameson[11] and using the point-implicit source term approach of Melson.[12]

III. Rotor Modeling

In this section we highlight the salient features of the rotor model which is described in detail in our previous work.[8] The rotor's effect on the flowfield is implemented through the body force source term in equation (1), permitting arbitrarily oriented rotors embedded in the computational volume mesh as compared to a boundary condition approach which must have grid aligned rotors. Rather than using an embedded polar mesh, we use the existing Cartesian cells to represent the rotor. Figure 1 shows the Cartesian hexahedra that contain the rotor disk plane, or "rotor hexes," on a coarse mesh. The rotor force in each hex is either prescribed using a fixed loading distribution (actuator disk) or coupled to the flow solution using blade element theory, in which the CFD velocity field determines the local angle of attack, from which the sectional lift and drag forces are computed from airfoil table lookups.

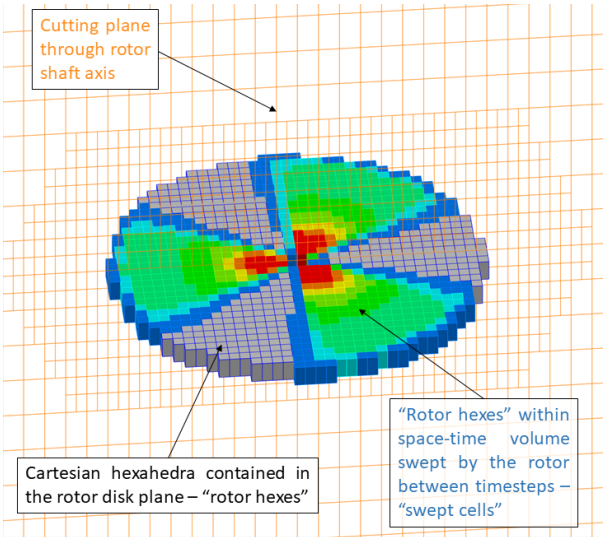

Figure 1: Diagram of rotor model showing mesh cutting plane, rotor hexes, and swept cells colored by scale factor

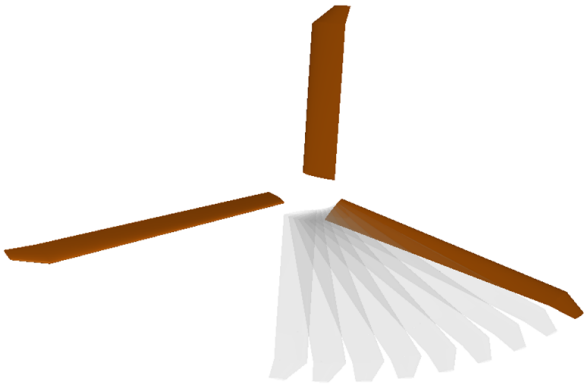

Figure 2: Example three-bladed rotor showing swept space-time volume of one blade between two instances in time

The rotor hexes utilize careful geometric definitions to improve the mapping of the cylindrical rotor segments to Cartesian hexahedra. In particular, the models in the literature scale the rotor forces by the

angular width ($\Delta\Psi$) of each cell.[13,14] However, for a Cartesian cell, we compute the scale factor (f_{sc}) as follows:

$$f_{sc} = \frac{N_b\,\Delta\psi}{2\pi} = \frac{N_b\,\Delta\psi}{2\pi}\frac{r\Delta r}{r\Delta r} = \frac{N_b A_c}{A_a} \tag{4}$$

where A_c is the area of the rotor disk plane inside the hex, A_a is the area of the annulus, $\Delta\psi$ is the azimuthal span of the cell, r is the cell's radial position, and Δr is the cell's radial span, defined as the diameter of a circle whose area is A_c.

The model smoothly transitions between steady and time-accurate modes by distributing the rotor forces over the entire space-time volume swept by the blade during a computational timestep. Figure 2 shows a representative three-bladed rotor and several translucent snapshots of one blade's position at previous instances in time. We apply forces to all of the rotor hexes touched by a blade between two timesteps, denoted by the colored hexes in figure 1 and called "swept cells." By virtue of using a rotating source term on a fixed computational mesh, the Cartesian cells intersecting the rotor disks are identified in one parallel-preprocessing step before the flow solution commences. The rotor hexes are then distributed among all available compute threads for parallel efficiency. The model showed good mesh convergence when each rotor comprised at least 10,000 rotor hexes.

The performance of the model was previously evaluated in hovering flight for both isolated and quadrotor configurations. In this work, the model is first validated for edgewise forward flight and then applied to quadrotor configurations to assess aerodynamic interactions among the rotors. The model is used in blade element mode for all simulations presented herein.[8]

IV. Computational Results

A. Validation Study: Isolated XV-15 Rotor in Edgewise Flight

As an initial evalution of the model in forward flight, an isolated XV-15 rotor was simulated at an advance ratio of 0.17 for a range of shaft angles (α_s) and compared to experimental data from a wind tunnel test in the 80x120 wind tunnel at NASA Ames Research Center.[15] The rotor was assumed to be planar and rigid and neither the rotor test apparatus (RTA) nor wind tunnel wall geometry were modeled. Cyclic pitch inputs were taken from the test data report while collective pitch was adjusted to match the desired thrust.

The computational mesh contained 18 million cells and the rotor was enclosed in a refinement region extending $1D$ upstream, $1.8D$ downstream, $1D$ laterally, and $0.6D$ below the rotor, where D is the rotor diameter. Approximately 50,000 hexes composed the rotor disk and the computational domain extended $30D$ away from the rotor except for the downstream boundary which was placed at $90D$. A representative solution showing the mesh and thrust force of each rotor hex is shown in Figure 3.

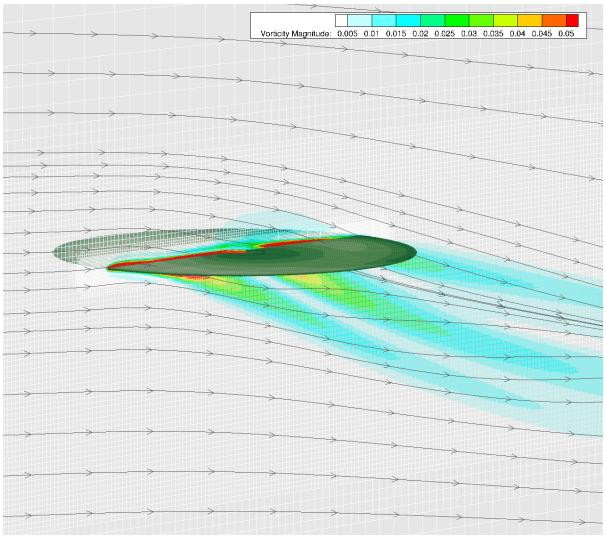

Figure 3: XV-15 isolated rotor in forward flight

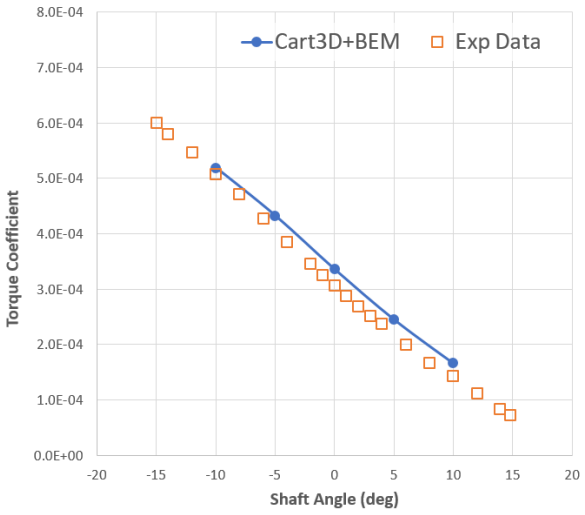

Figure 4: C_q vs α_s of XV-15 rotor, $C_T/\sigma = 0.075$

The variation of rotor power with shaft angle is well predicted overall, as shown in Figure 4. There

is a slight offset between the computational and experimental results which may be caused by modeling differences. *In the final paper, we will assess the effects of some of these differences, such as modeling of the RTA, wind tunnel walls, and non-planar rotor dynamics.*

B. Tandem Rotor Configuration

In the final paper, we will simulate the simple tandem rotor configuration of Huston[16] and compare rotor thrust and power predictions. Figure 5 shows the geometry, mesh, and centerline vorticity magnitude from a preliminary solution.

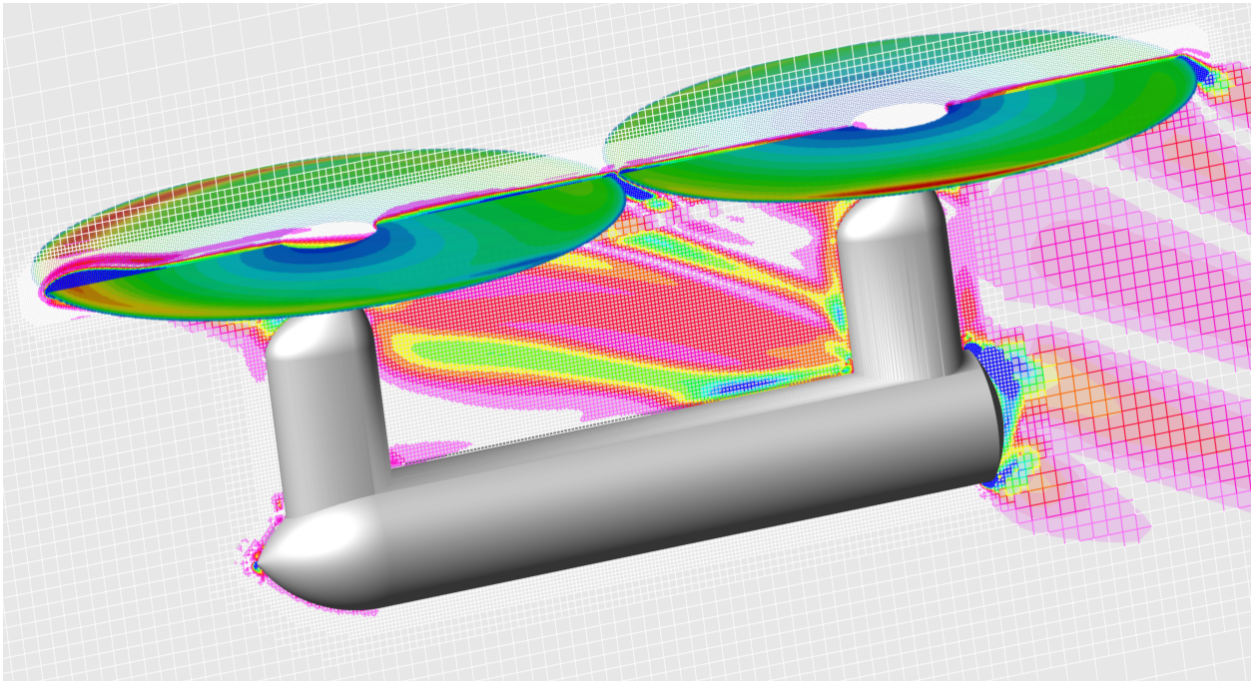

Figure 5: Example solution of tandem configuration[16] showing vorticity magnitude along centerline

C. Quadrotor Configurations

We begin our aerodynamic analysis of quadrotor configurations with a simple geometry using conventional rotor positions. Both "+" and "×" configurations are considered. Figure 6a shows the geometry for the "+" configuration, consisting of an ellipsoidal centerbody, four 12-inch long arms with a constant, square cross section, and cylindrical "motors." The centerbody's principal semi-axes are 5, 5, and 2.5 inches, while both the arm width and motor diameter are 1 inch. The motor rotation directions for the "+" configuration are shown in Figure 6b. For the "×" arrangement, the geometry is rotated 45 degrees, and the refinement regions are translated to the new motor positions, as shown in Figure 7.

The farfield boundaries are placed 30 arm lengths (36 propeller diameters) away in each Cartesian direction. As shown, grid refinement regions enclosing each rotor were used to better capture the shed vorticity of the vehicle. All simulations were performed at $M_\infty = 0.06$ ($\mu = 0.25$) and $\alpha = -5$ degrees. Figures 6a & 7a show the geometry and two orthogonal cuts through the ellipsoid center revealing the Cartesian mesh (19 million cells total).

1. Airframe Comparison

First, the "×" and "+" airframes are compared with no rotors. Vorticity iso-surfaces are shown for both configurations in Figure 8, where the vortex shedding of square arms is readily apparent. The "+" configuration has approximately 16% more drag than the "×" layout because of its larger projected cross-sectional area. *For the final paper, both steady and unsteady runs for each frame will be performed at several angles of attack.*

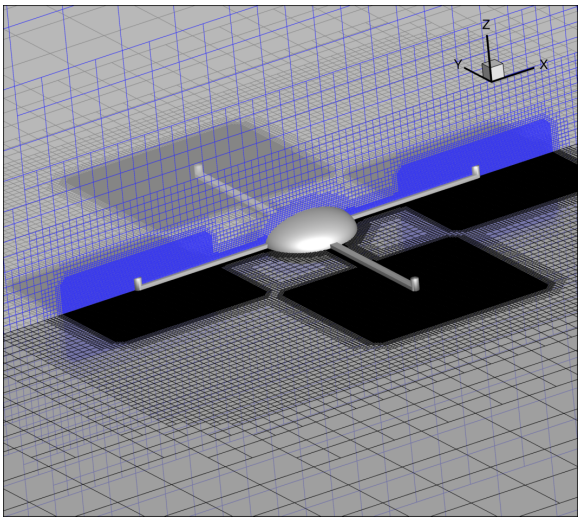

(a) Quadrotor geometry and mesh of "+" configuration with centerline (blue) and vertical (black) slices

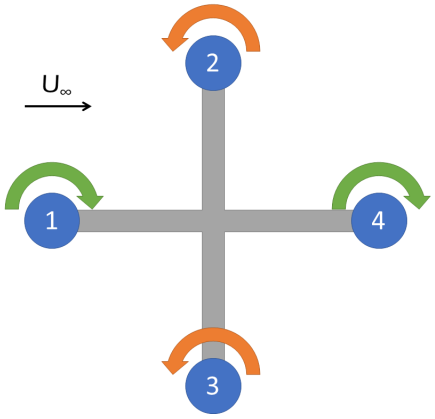

(b) Motor numbers and rotation directions for "+" configuration

Figure 6: Computational geometry, mesh, and motor rotation directions for "+" configuration

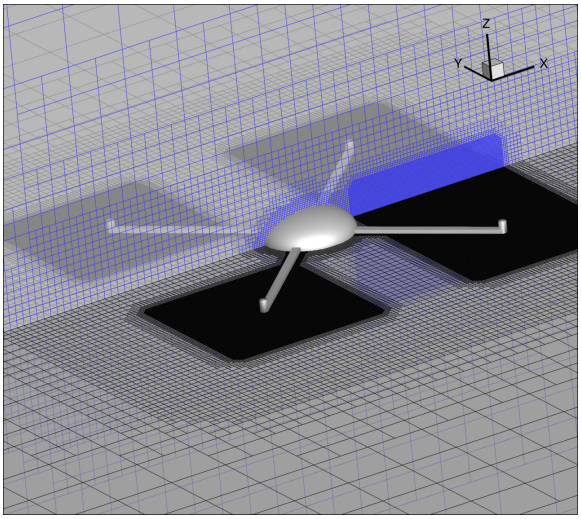

(a) Quadrotor geometry and mesh of "×" configuration with centerline (blue) and vertical (black) slices

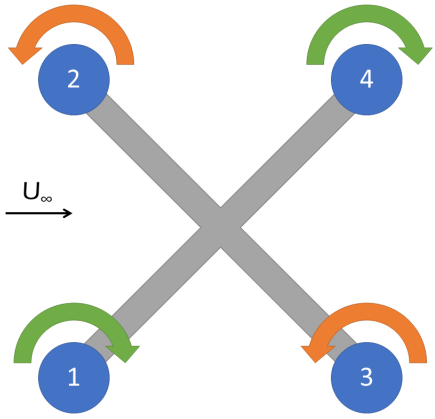

(b) Motor numbers and rotation directions for "×" configuration

Figure 7: Computational geometry, mesh, and motor rotation directions for "×" configuration

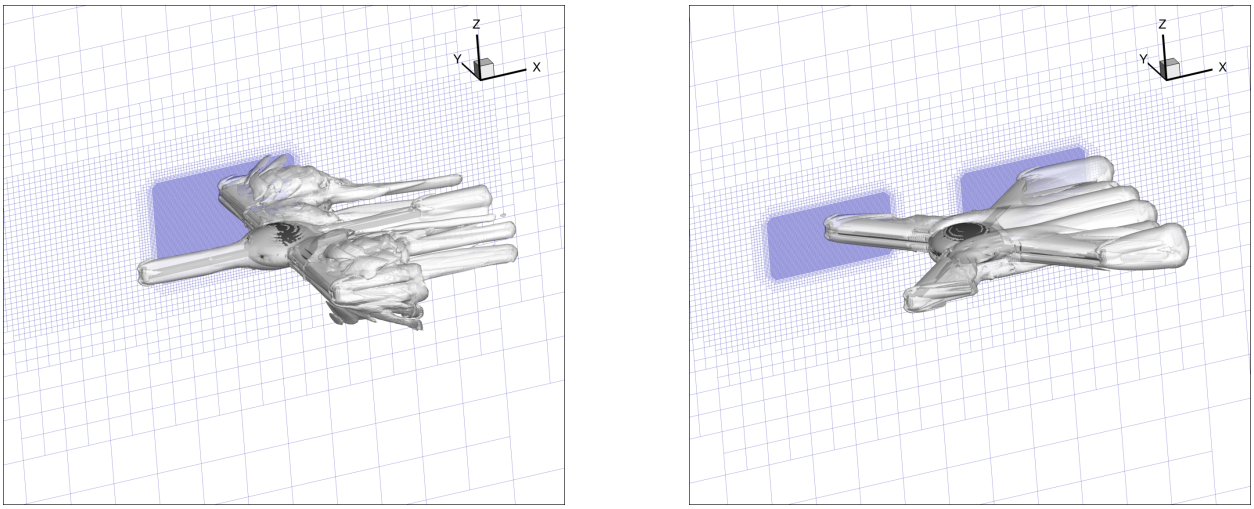

Figure 8: Vorticity iso-surface for "+" (left) and "×" (right) airframes, $|\omega| = 0.0125$

2. *Quadrotor "×" and "+" Configurations*

Next, the "×" and "+" configurations are simulated with the steady rotor model. The propeller planform and airfoils are scaled from the XV-15 proprotor to a 10-inch diameter, although the full-scale airfoil tables are retained for simplicity. *In the final paper, we will assess the effects of using airfoil tables at lower Reynolds numbers.* The tip Mach number is 0.24 which corresponds to an angular velocity of approximately 6000 rpm. Thrust was varied by adjusting the collective pitch keeping advance ratio constant for each rotor.

Figure 9 shows the vorticity iso-surfaces ($|\omega| = 0.0125$) for each configuration at a collective pitch (θ_{75}) of 10°. In forward flight, we see the leading rotor(s) generating the expected tip vortices, but the interaction of those vortices with the airframe and trailing rotors is complex.

The computed flowfields are qualitatively similar to that of Hwang, Jung, & Kwan, who used an unstructured URANS solver with discrete blade geometry.[7] *The final paper will include more detailed comparisons with Hwang, et al. such as thrust variation for individual rotors between the configurations. In addition, we will run time-accurate simulations with the unsteady rotor model and assess how the interactional aerodynamics in our model change with discrete tip vortices.*

In Figure 10 we see that the "+" configuration generates approximately 8% more thrust than the "×" configuration for the same conditions, which matches the numerical results of Hwang, et al. We believe, as they also concluded in their analysis, that this results from reduced aerodynamic interference for the forward rotors (1, 2, & 3) as compared to the "×" arrangement where rotors 3 & 4 fly in the wake of the upstream rotors. *In the final paper, we will analyze the thrust on each individual rotor for both configurations in detail and confirm this hypothesis.* We see that the thrust increase comes without a commensurate power increase, and so the quadrotor efficiency, as measured by L/D_e (for the rotors only), also increases for the "+" configuration, where $L = T\cos(\alpha)$ and $D_e = P/U_\infty$. *Since the "×" fuselage has less drag, we will compare complete vehicle forces (i.e. both rotor and airframe) in the final paper to assess the resultant performance differences between the two configurations. Comparisons between the steady and unsteady rotor models will also be reported in the completed manuscript.*

It is worth mentioning that, although less efficient aerodynamically, other design considerations could drive one towards an "×" configuration, such as camera field-of-view or roll authority requirements. *In addition, the vehicle is not in a trimmed configuration and further analysis will be performed for the final paper to determine how that affects these performance results.*

3. *Variations on Quadrotor "+" and "×" Configurations*

Finally, we simulate a variant of the "+" configuration where the side rotors (rotors 2 & 3, Fig 6b) are moved inboard by 25%. While this configuration (denoted "+′") creates additional complexity from a dynamics and controls perspective, it could potentially increase the aerodynamic benefit from the upstream rotor's

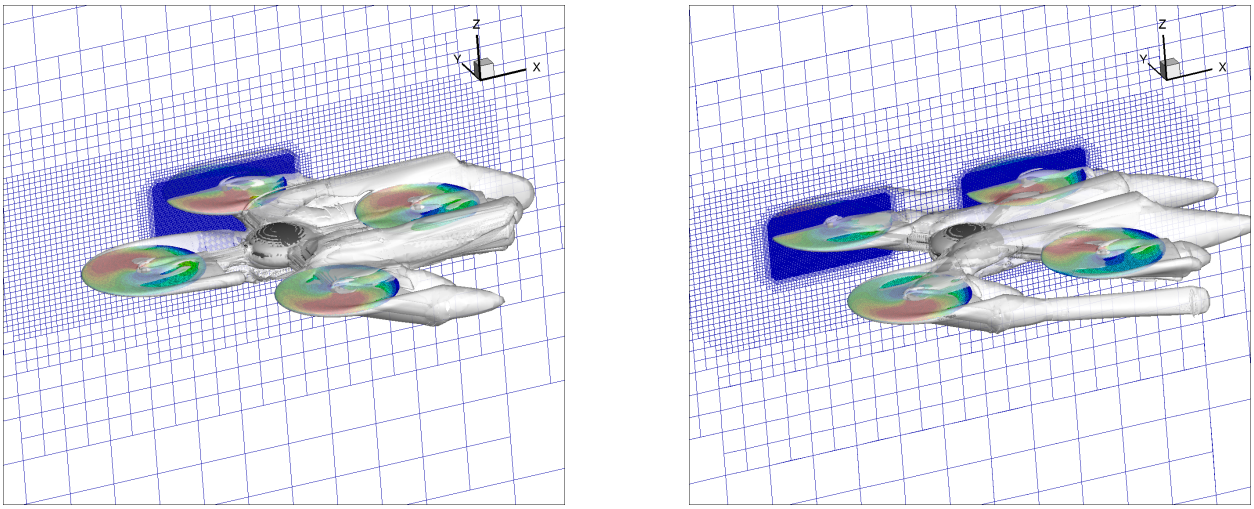

Figure 9: Vorticity iso-surface for "+" (left) and "×" (right) configurations: $\theta_{75} = 10°$, $|\omega| = 0.0125$

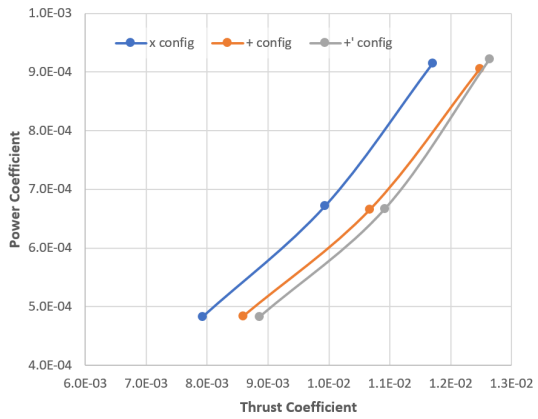

Figure 10: Thrust vs Power for several quadrotor configurations

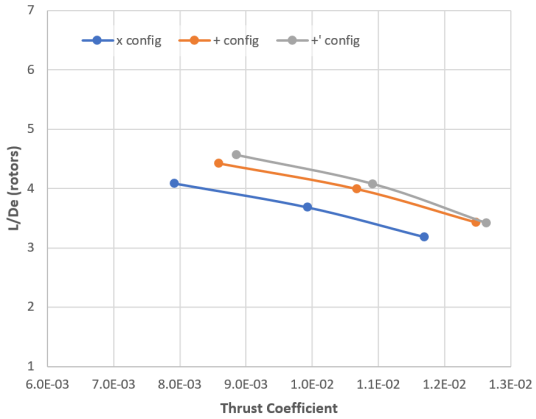

Figure 11: Thrust vs L/D_e (rotors only) for several quadrotor configurations

trailing vortices. It is important to remember that for a quadcopter, no individual rotor is trimmed (to zero moments) and thus the spanwise lift distribution (and therefore tip vortices) is (are) laterally asymmetric.

Figure 12 shows a comparison of vorticity iso-surfaces and thrust coefficient computed by each rotor hex between the "+" and "+′" configurations. The primary difference appears to be mild attenuation of the vortex shedding of the lateral arms. Referring back to figures 10 & 11, we see that total rotor performance is slightly better $(2 - 3\%)$ for the "+′" configuration, as thrust increases slightly while power remains constant. *As in the previous section, we will include full vehicle performance comparisons to assess the net change in overall performance as well as unsteady simulations in the final paper. In addition, we will investigate the differences between these two configurations at the highest collective* $(12°)$ *where the performance benefit disappears. Lastly, we will also assess a variant of the* "×" *configuration with the rear rotors moved outboard.*

V. Conclusions

In this abstract, we briefly review the development of a conservative, blade-element rotor model which has been implemented in an adaptive Cartesian mesh framework directed at flow simulations over complex geometries. We then apply the model, which was previously validated for multi-rotor simulations in hover, to rotors in edgewise forward flight. Performance predictions for an isolated rotor showed good correlation with wind tunnel data. Simulations of a quadcopter in forward flight were performed in two configurations, and the

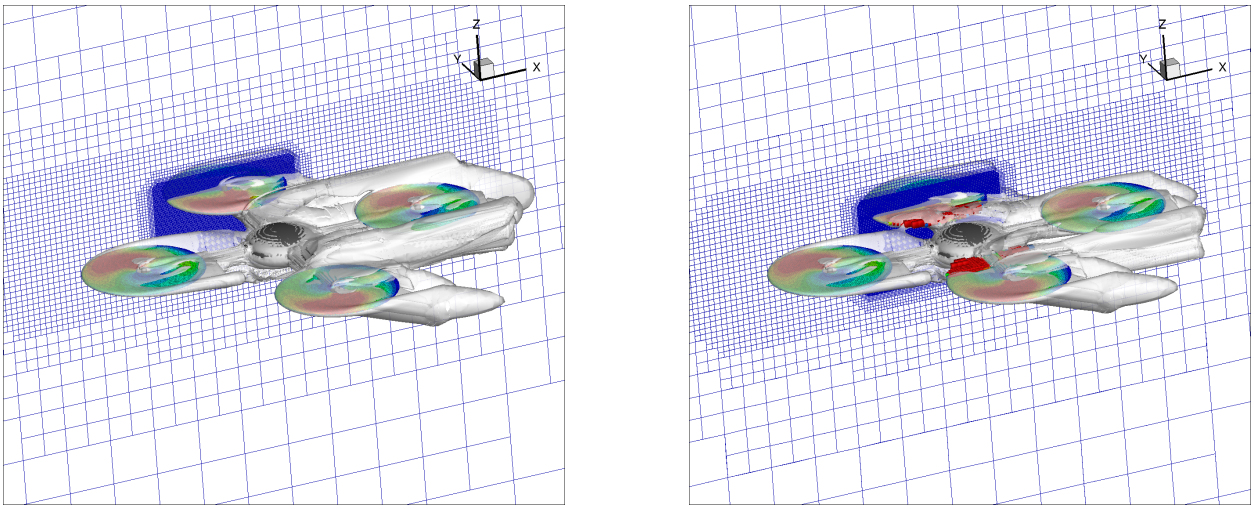

Figure 12: Vorticity iso-surface for "+" (left) and "+′" (right) configurations: $\theta_{75} = 10°$, $|\omega| = 0.0125$

rotors in a "+" configuration were found to be about 8% more efficient than in an "×" orientation because of reduced aerodynamic interference on the downstream rotors. We also analyze a modified "+" configuration where the lateral rotors are moved inboard 25%. This "+′" rotor arrangement shows a further 2% gain in rotor performance. Finally, we see that the model qualitatively matches high-fidelity URANS simulation results of a comparable configuration. *In the final paper, we will analyze full vehicle performance for each configuration, aerodynamic interference effects on individual rotors, and assess configuration performance with our unsteady rotor model. In addition, we will also assess a fourth configuration ("×′") where the rear rotors on the "×" configuration are moved outboard.*

Acknowledgments

This work was supported by the NASA Ames Research Center contract NNA10DF26C. The authors gratefully acknowledge the assistance of Jasim Ahmad and Tom Pulliam from NASA Ames. Computing resources were provided by the NASA Advanced Supercomputing division at Ames.

References

[1]Winslow, J., Hrishikeshavan, V., and Chopra, I., "Design Methodology for Small Scale Unmanned Quadrotors," *55th AIAA Aerospace Sciences Meeting*, 2017, p. 0014, AIAA 2017-0014.

[2]Botero, E. and Alonso, J. J., "Conceptual Design and Optimization of Small Transitioning UAVs using SUAVE," *18th AIAA/ISSMO Multidisciplinary Analysis and Optimization Conference*, 2017, p. 4149, AIAA 2017-4149.

[3]Yoon, S., Lee, H. C., and Pulliam, T. H., "Computational Analysis of Multi-Rotor Flows," 54th Aerospace Sciences Meeting, San Diego, CA, 2016, AIAA 2016-0812.

[4]Zhou, W., Ning, Z., Li, H., and Hu, H., "An Experimental Investigation on Rotor-to-Rotor Interactions of Small UAV," *35th AIAA Applied Aerodynamics Conference*, 2017, AIAA 2017-3744.

[5]Kaya, D., Kutay, A. T., and Tekinalp, O., "Experimental Investigation of Optimal Gap Distance between Rotors of a Quadrotor UAV," *AIAA Atmospheric Flight Mechanics Conference*, 2017, AIAA 2017-3894.

[6]Luo, J., Zhu, L., and Yan, G., "Novel quadrotor forward-flight model based on wake interference," *AIAA Journal*, Vol. 53, No. 12, 2015, pp. 3522–3533.

[7]Hwang, J. Y., Jung, M. K., and Kwon, O. J., "Numerical study of aerodynamic performance of a multirotor unmanned-aerial-vehicle configuration," *Journal of Aircraft*, Vol. 52, No. 3, 2014, pp. 839–846.

[8]Chiew, J. J. and Aftosmis, M. J., "A Conservative, Scalable, Space-Time Blade Element Rotor Model for Multi-rotor Vehicles," *AHS Aeromechanics Design for Transformative Vertical Flight, San Francisco, CA*, 2018, Abstract accepted.

[9]Aftosmis, M. J., Berger, M. J., and Adomavicius, G., "A parallel multilevel method for adaptively refined Cartesian grids with embedded boundaries," 38th Aerospace Sciences Meeting, 2000, AIAA 2000-0808.

[10]Aftosmis, M. J., Berger, M. J., and Melton, J. E., "Robust and efficient Cartesian mesh generation for component-based geometry," *AIAA journal*, Vol. 36, No. 6, 1998, pp. 952–960.

[11]Jameson, A., "Time dependent Calculations Using Multigrid, with Applications to Unsteady Flows Past Airfoils and Wings," 10th Computational Fluid Dynamics Conference, Jun 1991, AIAA 1991-1596.

[12]Melson, N., Sanetrik, M., and Atkins, H., "Time-accurate Navier-Stokes Calculations with Multigrid Acceleration," *Sixth Copper Mountain Conference on Multigrid Methods*, Copper Mountain, CO, Apr 1993.

[13]Tadghighi, H., "Simulation of rotor-body interactional aerodynamics- An unsteady rotor source distributed disk model," AHS International 57th Annual Forum, 2001.

[14]O'Brien Jr, D. M., *Analysis of computational modeling techniques for complete rotorcraft configurations*, Ph.D. thesis, Georgia Institute of Technology, 2006.

[15]Light, J. S., "Results from an XV-15 rotor test in the National Full-Scale Aerodynamics Complex," *AHS 53rd Annual Forum, Virginia Beach, VA*, 1997, pp. 231–239.

[16]Huston, R. J., "Wind-tunnel Measurements of Performance, Blade Motions, and Blade Air Loads for Tandem-Rotor Configurations With and Without Overlap," 1963, NASA TN D-1971.